

## Article

# Experimental Evaluation of Conjugate Flaws on Rock Dynamic Fracturing

Ziyun Li <sup>1,\*</sup>, Song Xie <sup>1</sup>, Qianghui Song <sup>2</sup>, Peiyong Wang <sup>2</sup>, Dongyan Liu <sup>3,4</sup> and Kaixi Xue <sup>5</sup>

<sup>1</sup> Chongqing Key Laboratory of Energy Engineering Mechanics and Disaster Prevention and Mitigation, Chongqing University of Science and Technology, Chongqing 401331, China

<sup>2</sup> Chongqing Key Laboratory of Geomechanics & Geoenvironment Protection, Army Logistics Academy, Chongqing 401311, China

<sup>3</sup> School of Civil Engineering, Chongqing University, Chongqing 400044, China

<sup>4</sup> Architectural and Engineering Institute, Chongqing College of Architecture and Technology, Chongqing 401331, China

<sup>5</sup> School of Civil and Architecture Engineering, East China University of Technology, Nanchang 330013, China

\* Correspondence: ziyun.li@cqust.edu.cn

**Abstract:** The fracture behaviors of rocks under dynamic loading are significantly affected by flaws. Understanding regarding this fundamental mechanism of flaw-induced dynamic fracturing could aid in reducing dynamic geohazards in deep rock engineering. In this study, a series of dynamic loading experiments are conducted on conjugate flawed white sandstone specimens to study the effect of the geometric configuration of flaws on dynamic fracturing. The results show that the geometry configuration of flaws and the loading conditions both strongly affect cracking and failure behaviors. Two types of shear cracks and three types of tensile cracks are observed, four coalescence patterns are identified, and the global failure modes of rock are usually coupled with two or more coalescence patterns. The inhibiting and enhancing mechanism of flaws in regards to potential shear fracture are obtained. These two failure mechanisms depend on the angular relationship between the flaws and the potential shear strain field. The “guiding effect” of the flaws results in the deviation and deformation of shear cracks. Moreover, it is found that the loading condition dominates the fracture tendency of rock macroscopically, while the geometric setting of flaws significantly affects the fracture behavior and failure mode locally.

**Keywords:** deep underground engineering; failure mechanism; conjugate joints; rock dynamic



**Citation:** Li, Z.; Xie, S.; Song, Q.; Wang, P.; Liu, D.; Xue, K. Experimental Evaluation of Conjugate Flaws on Rock Dynamic Fracturing. *Sustainability* **2023**, *15*, 3637. <https://doi.org/10.3390/su15043637>

Academic Editor: Ashraf Dewan

Received: 29 January 2023

Revised: 14 February 2023

Accepted: 14 February 2023

Published: 16 February 2023

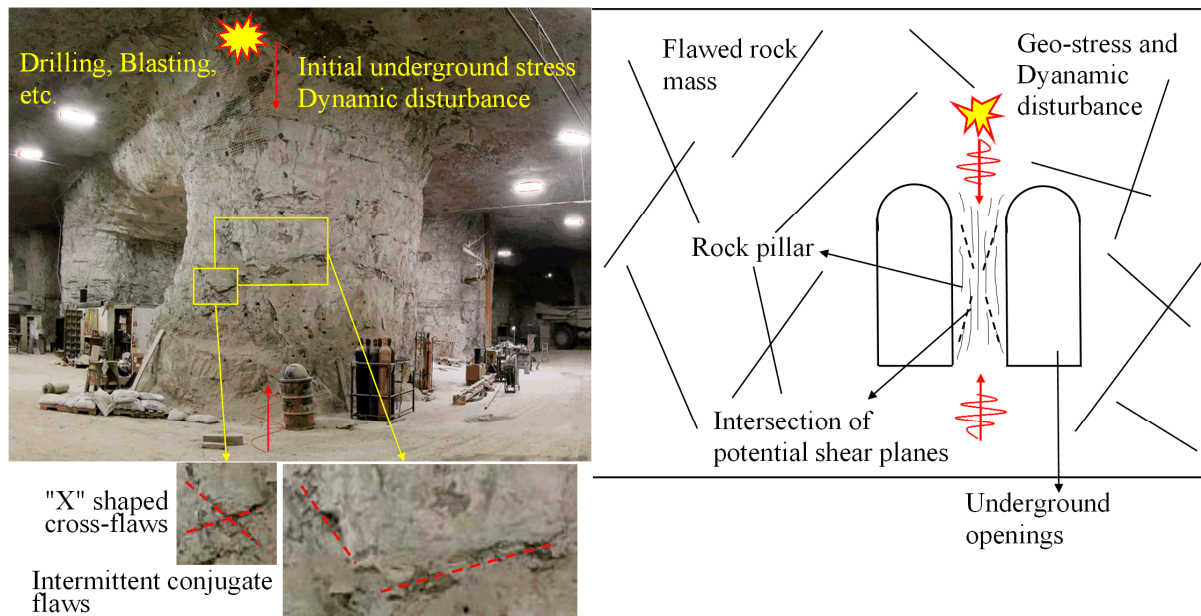


**Copyright:** © 2023 by the authors. Licensee MDPI, Basel, Switzerland. This article is an open access article distributed under the terms and conditions of the Creative Commons Attribution (CC BY) license (<https://creativecommons.org/licenses/by/4.0/>).

## 1. Introduction

The intersection or coalescence of multiple groups of original flaws under geological movements or engineering activities generally results in widely distributed conjugate-shaped persistent and non-persistent defects [1–4], such as the rock pillar illustrated in Figure 1. When subjected to the combined influence of in situ stress and external dynamic stress (drilling, blasting, excavation, vibration, etc.), new cracks usually emerge at the non-persistent flaw tips, then extend across the rock bridge, and coalesce with other flaws, ultimately forming X-shaped cross-flaws. In geology, conjugate joints generally refer to the fractures formed by the shear stress of rock, which are also known as X-shaped joints, a type of shear joint. The conjugate joints are developed simultaneously on two sets of intersecting shear planes; the intersection angles and the development degree of the conjugate joints may vary under different geological conditions. The distribution patterns of conjugate non-persistent defects and their intersections affect the fracturing behavior of the rock material and dominate the stability of the local rock mass [3]. Deep underground mining processes, with dynamic disturbances, could result in dynamic disasters in a flawed rock mass. Understanding the dynamic crack coalescence and failure mechanism of a conjugate

flawed rock mass under dynamic loading is of vital significance to the stability evaluation and hazard control in underground rock engineering applications.

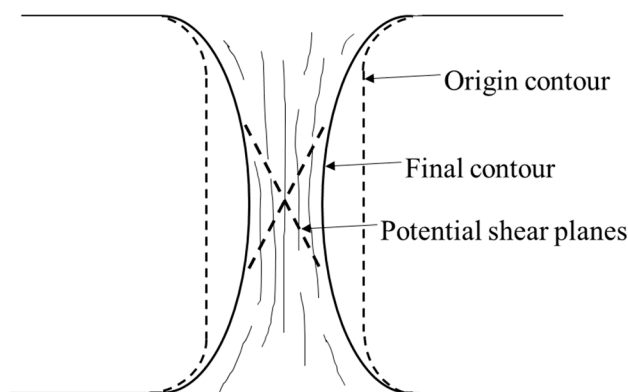


**Figure 1.** Schematic of the underground rock mass with conjugate potential shear planes subjected to geo-stress and dynamic loading.

The fracture propagation leading to rock failure is an important topic in rock mechanics research [1]. The initial geometric distribution of flaws and stress loading conditions are the main factors that influence the cracking coalescence paths and rock failure modes. Extensive efforts extended the investigation on the crack intersection behaviors of rock with various configurations of flaw settings. The studies on crack coalescence involving flaw settings include three flaws [5] and two flaws, arranged in different geometries [6–8], dissimilar layers with parallel joints [9], non-parallel flaws subjected to uniaxial compression [10,11], ubiquitous joints [12], parallel flaws [13], cross-flaws [14], unfilled and filled flaws [15]. Numerous studies have demonstrated that fracture behavior under dynamic loading is significantly different from that under quasi-static loading conditions. The fracture behavior of rock under quasi-static loading conditions has been studied comprehensively. Zhou et al. [16] investigated the fracture behavior of multi-flawed rocks by means of digital image correlation, Cao et al. [17] studied the crack propagation and coalescence of cracks, and Wong R et al. [18] briefly described the shear zone formation in brittle solids under compressive stresses. Wong LNY et al. [19] made microscopic observations and interpretations regarding the crack coalescence in molded gypsum and Carrara marble.

Under dynamic loading, the mechanical properties, energy characteristics, fracturing behaviors, and failure modes of flawed rocks with various flaw configurations were also extensively investigated. These studies focused on flaw configurations settings, including noncoplanar and unparallel flaws [20], single and multiple flaws [21–24], and stress conditions such as loading rate and pre-compressed stress state [25,26]. Feng et al. [27] investigated the effects of the dynamic strain rate on the energy dissipation and fragment characteristics of cross-fissured rocks. Many scholars conducted dynamic and coupled static-dynamic tests on rocks or rock-like specimens with multiple flaws or other defects [28–30]; the results indicate that the flaw settings and loading conditions affect the mechanical property, fracturing behavior, and energy evolution of pre-flawed rock [31,32]. Specifically, the effects of strain rate and pre-stress level on fracturing behaviors and the failure modes of flawed rock were discovered [33–35]. The progressive fracturing behaviors of coplanar elliptical flaws have also been studied from macro, meso, and micro view-

points [36]. Note that the flawed rock specimens in existing studies are usually arranged regularly as one set with the same angle. However, multi-set flaw modes are common in nature, and their geometric distributions have a strong influence on crack coalescence patterns [3]. The crack coalescence behaviors of rock mass with conjugate flaws have not been thoroughly studied. For instance, in the commonly seen spalling and shear faulting of mine pillars, shown in Figure 2 [11], the intersection process of the conjugate shear planes remains unstudied.



**Figure 2.** Spalling and shear faulting of mine pillars [11].

The rock masses in deep underground engineering are simultaneously subjected to in situ geo-stress and dynamic disturbance. However, the previous studies on crack coalescence and failure mechanisms mainly focus on either flawed rock subjected to quasi-static or individual dynamic loading. Meanwhile, the influences of conjugate flaws on the failure mechanism of rock remains unknown. It is essential to acquire the fracturing behavior of conjugate flaws subjected to dynamic loading. In this paper, experimental studies are conducted, incorporating the effect of the non-persistent geometric settings of flaws and dynamic loading, to explore the crack coalescence behaviors and failure mechanism of non-persistent conjugate-flawed rock. The fracturing process and failure modes of rock are captured by a high-speed camera. The influence of flaw geometric settings, loading conditions, and static pre-stress levels on crack coalescence behavior and failure mechanisms are discussed.

The research has theoretical significance in the following areas: problems regarding jointed rock mass stability evaluation in practical engineering, i.e., slender rock pillars in mines, and fracture mechanics with non-persistent multiple flaws. Our study provides observations and analysis of the whole fracturing process, including crack propagation through rock bridges, crack coalescence, and ultimate failure modes under coupled static-dynamic loading. Moreover, the coalescence between non-persistent multiple flaws is commonly seen in the fracture of all kinds of brittle materials, which could draw inspiration from this study.

## 2. Experimental Methodology

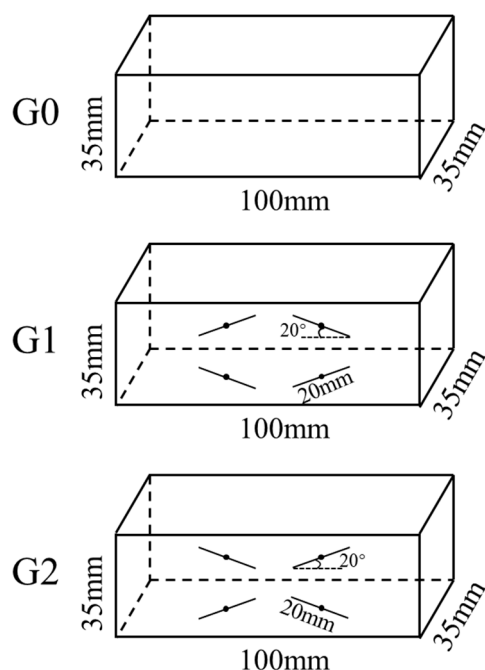
### 2.1. Specimen Preparation and Testing Scheme

An intact white sandstone block from Neijiang, Sichuan Province of China, with good geometrical integrity and petrographic uniformity, was selected, and rectangular cuboid samples, with an average length, width, and thickness of 100 mm, 35 mm, and 35 mm, respectively, were cut from this block. The specimen surfaces were carefully polished, with roughness less than 0.02 mm, in accordance with the requirements of the International Society for Rock Mechanics (ISRM) [37]. The basic physical and mechanical properties of the white sandstone are listed in Table 1. Cylindrical specimens, with a diameter of 50 mm and an aspect ratio of 2:1, and Brazilian disc specimens, with a geometry of 50 × 25 mm (diameter × thickness), were used to test the UCS and the indirect tensile strength, respectively.

**Table 1.** Physical and mechanical properties of white sandstone.

Density (kg/m <sup>3</sup> )	Young's Modulus E/GPa	Poisson's Ratio $\nu$	UCS/MPa	Brazilian Tensile Strength/MPa	Longitudinal Wave Velocity/(m/s)
2655.36	15.2	0.24	108.81	9.61	3440

There are two steps in the fabrication process of the flaws. Firstly, the specimen is punched with a drilling pit to obtain a hole of a diameter of 2 mm. Then, a diamond saw is used to cut through the small hole along the predetermined direction to fabricate non-persistent conjugate flaws in the length of 20 mm. The width and length of the flaws are 0.3–0.4 mm and 20 mm, respectively. In this study, three groups of specimens are divided. As shown in Figure 3, G0 represents intact specimens, G1 and G2 represent prefabricated-flawed specimens, and both are processed as non-persistent conjugate settings with four flaws. In particular, the four holes in the middle of the flaws in G1 and G2 were assigned fixed coordinate positions; the only difference between the two groups is that the inclination angles of the flaws are opposite. The absolute value of angles between horizontal direction and flaw orientation is 20°. Meanwhile, the gap between the inner flaw tips and the distance between the outer flaw tips and the edge of the specimen are the same in these two groups. It is worth noting that to eliminate or minimize the end effect, we set the length of the specimen up to 100 mm, with a 24 mm distance between the outer flaw tips and the edge of the specimen. The specimens were dried in a drying oven with a constant temperature of 105 °C for 24 h prior to testing.

**Figure 3.** The geometry of the three groups of rock samples with different flaw settings.

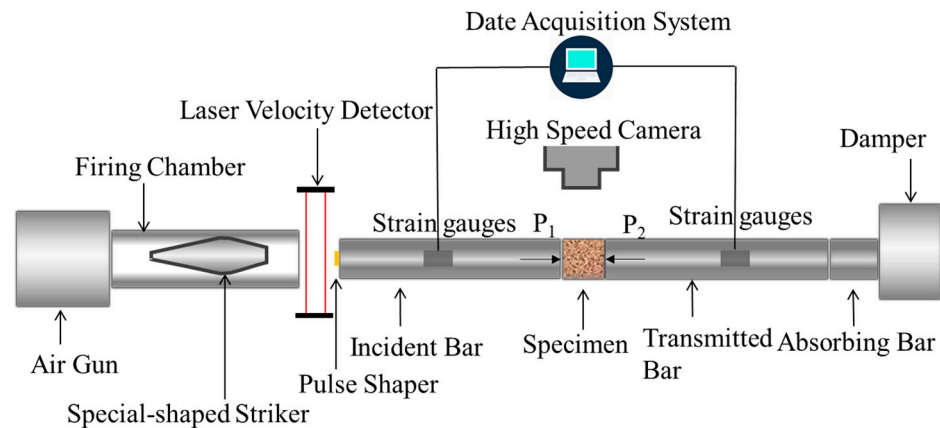
The static strengths and failure behaviors of three groups of rock samples were determined using an MTS793 rock testing system. The average UCSs for groups G0, G1, and G2 are 108.81 MPa, 58.31 MPa, and 70.22 MPa, respectively. In the coupled static-dynamic experiments, the ratio of the axial static pre-stress to the uniaxial compression stress (UCS) of the three groups of specimens is defined as the pre-stress level.

## 2.2. Experimental System and Procedure

The tests were conducted using a modified SHPB system in Central South University (Changsha, China), as illustrated in Figure 4. The system consists of a nitrogen-driven gas



gun, a cone-shaped striker (0.36 m in length), an incident bar (2 m in length), a transmitted bar (2 m in length), an absorbing bar (0.5 m in length), an axial confinement unit, a data acquisition device, and an image acquisition system [21]. The striker and bars are made of high-strength 40 Cr alloy steel. The diameter, elastic modulus, P-wave velocity, and density of the bars are 50 mm, 233 GPa, 5458 m/s, and 7810 kg/m<sup>3</sup>, respectively [35].



**Figure 4.** Schematic diagram of the SHPB system.

In the coupled static-dynamic loading experiments, the sample is first sandwiched between the incident bar and the transmitted bar. Vaseline is glued between the surfaces of the specimen and bars to minimize the end friction effect [37]. Then, the static pre-stress is applied to the predetermined pre-stress level. Subsequently, the cone-shaped striker is launched to impact the incident bar, generating a half-sine stress wave. When reaching the contact surface of the incident bar and the rock sample, the incident stress will be separated into transmitted stress and reflected stress. These three stress waves are recorded by the strain gauges fixed at the middle of the incident and transmitted bars. The image acquisition system was composed of two LED lights and a CMOS sensor-based high-speed camera (Phantom V711) with a Nikon AF Zoom-Nikkor 80–200 mm f/2.8D ED lens. The high-speed camera was set with a resolution of 256 × 128 pixels, and a frame rate of 50,000 frames per second (i.e., inter-frame time of 20 μs) [35]. By inflating different air pressures in the air chamber, the striker is pushed to strike the incident bar at different fixed speeds, and different loading rates are implemented.

### 2.3. Verifying the Stress Equilibrium State

Based on the one-dimensional stress wave theory, a stress equilibrium state is required prior to the rock sample's failure. That is, the sum of the incident stress and reflected stress should be almost equal to the transmitted stress before the peak stress. In this study, a half-sine incident wave for a duration of 250 μs is generated using a cone-shaped striker. The time for the incident stress wave to propagate from the right edge of the rock sample to the left is about 29 μs. After 116 μs, the incident wave has essentially propagated twice back and forth through the rock sample prior to the peak incident stress, and the relative value of the stress difference between the two ends is about 6%, and in this case, a constant dynamic loading rate and a dynamic stress equilibrium state are achieved for the rock sample.

In this study, we mainly focus on the dynamic fracturing behavior of rock influenced by the geometric configuration of conjugate flaws, rather than on the mechanical properties. Therefore, a maximum relative value of stress difference of 6% is acceptable; meanwhile, the fracture progress during dynamic loading shows good symmetry.

Figures 5 and 6 present the original waveforms and dynamic stress equilibrium check in this study (i.e., G0-30-0.3). The superposition of the incident stress and the reflected stress nearly coincide with the transmitted stress, especially prior to the peak stress, indicating

that the stress equilibrium state is achieved in the present experiments, and the validity of experimental results is verified.

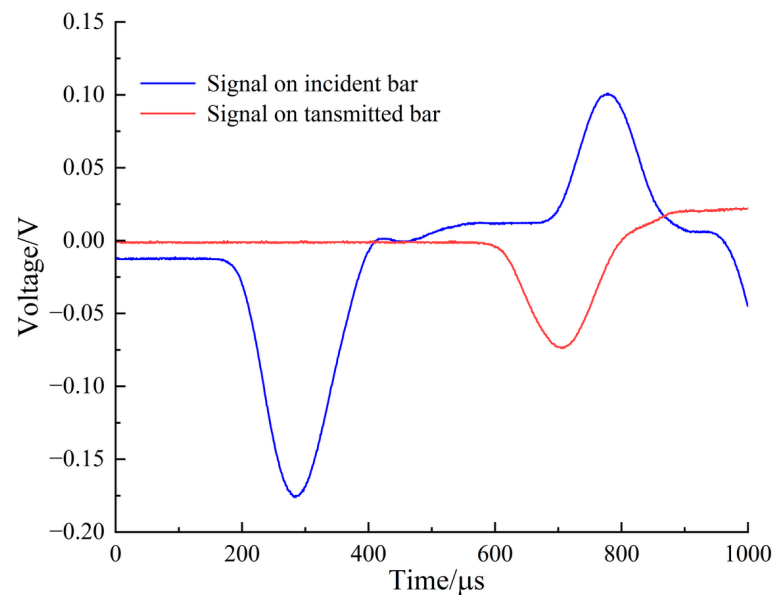


Figure 5. Original waveforms.

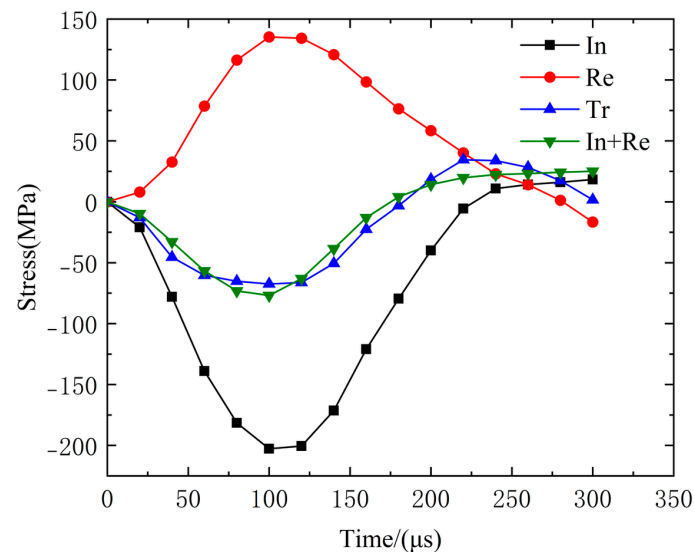


Figure 6. Verification of the dynamic stress equilibrium in the SHPB test in sample G0-30-0.3.

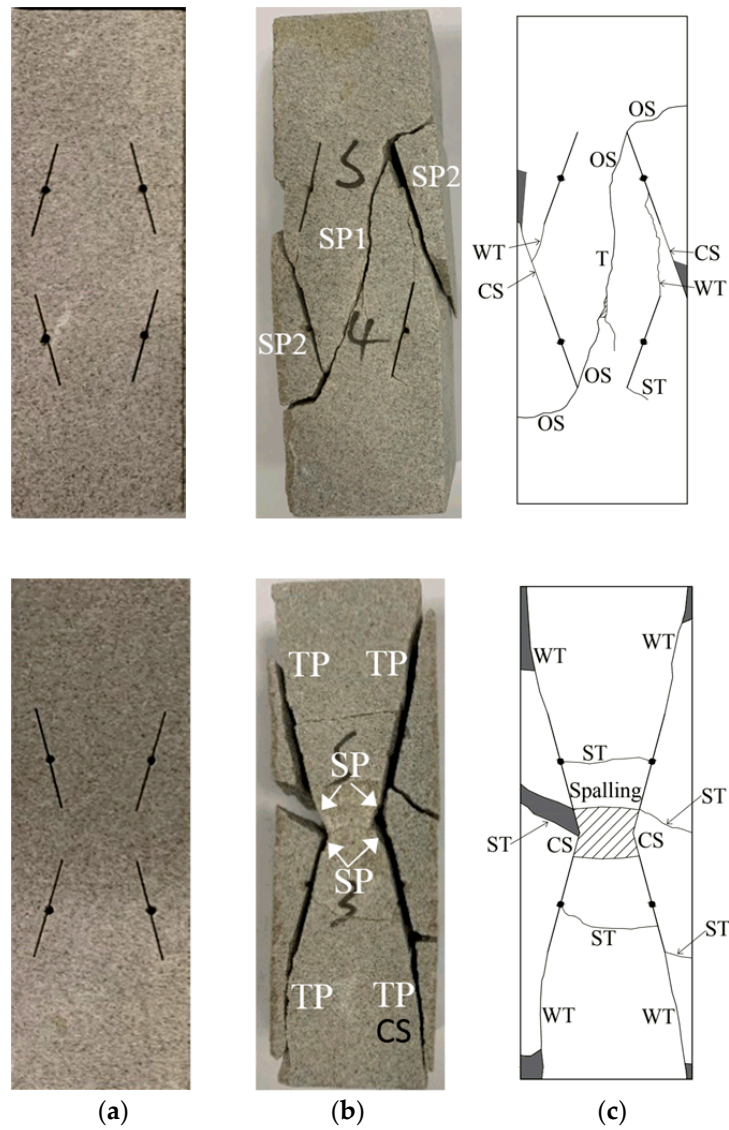
### 3. Experimental Results

#### 3.1. Fracturing Behaviors and Failure Modes Subjected to Quasi-Static Loading

The uniaxial compression strengths of rock samples in G0, G1, and G2 are 108.81 MPa, 58.31 MPa, and 70.22 MPa, respectively. Note that the strength values of the cylinder specimen and rectangular cuboid specimen are the same, regardless of the sample shape. The cylinder sample's failure mode is X-shaped shear failure, as seen in Figure 7. The fracturing behaviors and failure modes of the non-persistent conjugate-flawed specimens G1 and G2 are shown in Figure 8.



**Figure 7.** Failure image of cylinder white sandstone specimen under quasi-static loading (The loading direction is vertical).



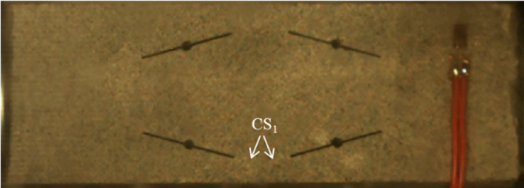

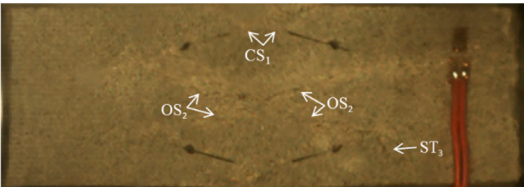
**Figure 8.** Comparison of the fracturing behaviors between G1 and G2: (a) flaw geometric settings, (b) failure modes, and (c) crack types and coalescence patterns (the loading direction is vertical).

Based on the experimental observations in Figure 8, four types of cracks—coplanar shear cracks (CS), oblique shear cracks (OS), tensile wing cracks (WT), and secondary tensile cracks (ST)—propagate at the flaw tips. These cracks are similar to those found by Wong et al., Zhao et al., Lin et al., Zhang et al., and Cao et al. [7–10,12] in uniaxial compression tests. G1 and G2 both fracture in the shear failure mode; however, the predominant shear crack types vary in their failures.

### 3.2. Dynamic Fracturing Behaviors

The fracturing behaviors of rock are different under different loading conditions and geometric flaw settings. Take the representative specimen G1-50-0.6 as an example. Table 2 depicts the crack types and fracturing behavior of flawed specimens under the pre-stress level of 50% and the  $1982 \text{ GPa}\cdot\text{s}^{-1}$  dynamic loading rate.

**Table 2.** Fracturing process of G1-50-0.6 specimen. (The loading direction is horizontal.)

Image	Pre-Stress (Percentage of UCS)/MPa	Loading Time/ $\mu\text{s}$	Cracking Sequence
	29.16 (50%)	100	Coplanar shear cracks emerge from the inner tips between the conjugate flaws.
		120	1. X-shaped conjugate shear cracks initiate between the outer tips. 2. Coplanar shear cracks run through the boundary.
		140	1. The four oblique shear cracks coalesce with each other, forming X-shaped conjugate shear bands. 2. Secondary tensile cracks are induced.

For each photograph, the dynamic loading direction is from the right side to the left side. Two types of shear cracks and three types of tensile cracks are observed and categorized in the experiments, i.e., coplanar shear cracks and oblique shear cracks initiated at the flaw tips, far-field tensile cracks emerged at the edge of the specimen, and wing cracks and secondary tensile cracks initiated at the flaw tips. The cracks are represented by the capital letters “CS”, “OS”, “FT”, “WT”, and “ST”, respectively, and the numbers represent the order in which each crack appears. The crack types of each specimen under different loading conditions are detailed in Supplementary Material.

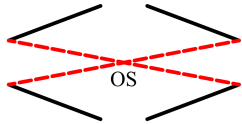
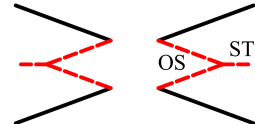
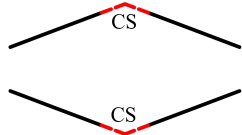
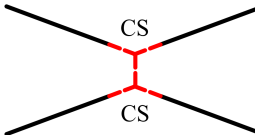
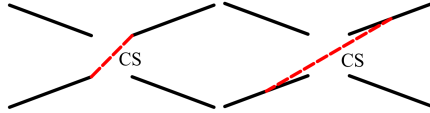
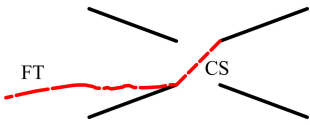
Table 2 presents the fracturing process of G1-50-0.6. Under coupled static-dynamic loading conditions, the coplanar shear cracks first emerge from the inner tips between the conjugate flaws and run through the boundary along the trajectories of the white patches, inducing a slight dilatancy effect and a spalling tendency. Subsequently, oblique shear cracks emerge at the outer flaw tips of the two pairs of parallel flaws, intersecting with each other in the middle, resulting in an X-shaped shear band. Afterward, far-field tensile cracks initiate at the edge of the specimen. However, this type of crack does not coalesce with

the flaws or other shear cracks. Upon relative sliding of the shear cracks, secondary tensile cracks are induced at the outer flaw tips. Under coupled loading conditions, a similar X-shaped conjugate shear band filled with pulverized rock powder appears in the center of the specimen, but no far-field tensile cracks are observed.

For brittle rock materials, crack coalescence plays a vital role in fracturing, and significantly influences the global failure mode. Therefore, the investigation of coalescing patterns of cracks subjected to different loading conditions may aid in furthering the understanding of the failure mechanism of non-persistent rock specimens.

Therefore, the investigation of coalescing patterns of cracks subjected to different loading conditions could help us to further analyze the failure mechanism of non-persistent conjugate-flawed rock specimens. According to the cracking process, four coalescence patterns are observed by means of a high-speed camera during the dynamic loading process, as illustrated in Table 3.

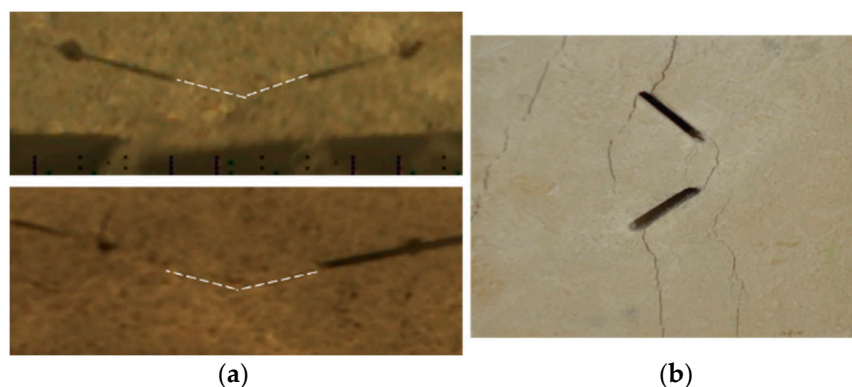
**Table 3.** Crack coalescence patterns. (The loading direction is horizontal.)

Crack Coalescence Patterns	Crack Coalescence Modes		Description	Specimen No.	
	G1	G2		G1	G2
I			Oblique shear crack coalescence between parallel or conjugate flaws.	G1-0-0.6 G1-30-0.3 G1-30-0.6 G1-50-0.3 G1-50-0.6	G2-50-0.6
II			Coplanar shear crack coalescence between conjugate flaws.	G1-0-0.3 G1-0-0.6 G1-30-0.3 G1-30-0.6 G1-50-0.3 G1-50-0.6	G2-0-0.3 G2-30-0.3 G2-30-0.6 G2-50-0.3 G2-50-0.6
III	-		Quasi-coplanar shear crack coalescence between parallel flaws.	-	G2-0-0.6 G2-30-0.6 G2-50-0.3
IV	-		Coalescence of far-field tensile crack and quasi-coplanar shear crack.	-	-

Pattern I: Oblique shear crack coalescence between parallel or conjugate flaws. The oblique shear cracks and dynamic loading direction intersect at a small angle. Both G1 and G2's main shear bands are X or half X-shaped. For G2, secondary tensile cracks are induced upon the coalescence between oblique shear cracks.

Pattern II: Coplanar shear crack coalescence between conjugate flaws. This pattern occurs between the conjugate flaws with proximity, which is observed in nearly every experiment. However, it dominates the global failure pattern of the specimen only under lower pre-stress and lower dynamic loading. The coplanar shear crack coalescence behavior under dynamic loading reveals a significant difference with regards to the mixed tensile-shear crack occurrence under uniaxial compression [10], as illustrated in Figure 9.





**Figure 9.** Crack coalescence between conjugate flaws: (a) subjected to dynamic loading (the loading direction is horizontal); (b) subjected to quasi-static loading (the loading direction is vertical).

**Pattern III: Quasi-coplanar shear crack coalescence between parallel flaws.** This pattern of crack coalescence is only observed in G2, which occurs between the inner tips or middle of two diagonally parallel flaws. Although there was an X-shaped white patch between the four conjugate inner flaw tips prior to cracking, shear cracks only occur subsequently between one pair of parallel flaws. When relative sliding occurs in the shear crack, secondary tensile cracks, with smooth and flat surfaces, are subsequently induced in the middle part of the shear belt. This mode of shear crack coalescence between two parallel flaws is consistent with the uniaxial compression tests obtained by Wong and the dynamic loading experimental results obtained by Yue [7,23].

**Pattern IV: Coalescence of far-field tensile crack and quasi-coplanar shear crack.** When specimen G2-0-0.6 is subjected to individual dynamic loading, a far-field tensile crack intersects with the main quasi-coplanar shear crack, resulting in mixed tensile-shear failure of the specimen. This coalescence pattern is not commonly seen under quasi-static loading conditions, where far-field tensile cracks scarcely appear.

The experimental results reveal that the fracturing behavior and crack coalescence pattern have a bearing on both geometric setting of the flaws and the loading condition. On the other hand, shear crack coalescence is more commonly seen under dynamic loading than quasi-static compression.

### 3.3. Failure Mechanism

The analysis of failure mode is an effective method for studying the failure mechanism of rock subjected to dynamic loading. The failure modes of each specimen under different loading conditions are detailed in Supplementary Material. The fracturing behaviors and failure modes of specimens under dynamic air pressure 0.5 MPa and 0.6 MPa are nearly the same. Therefore, for comparison purposes, only the failure mode diagrams of samples subjected to low (0.3 MPa) and high (0.6 MPa) dynamic loadings are displayed.

#### 3.3.1. Failure Modes of Specimens in Group G0

Under quasi-static compression, stress concentrations develop more easily, resulting in one major shear fracture occurring along the diagonal of the intact specimen. This is different from the splitting fracture behavior of typical brittle cylindrical rock. This may be due to the influence of the rectangular shape of the specimen section.

When subjected to individual high dynamic loading, the specimen shows typical tensile splitting behavior along one main cracking surface. While under coupled static-dynamic loading conditions, the conjugate X-shaped shear failure mode is observed with shear cracks extending along the diagonal direction.

### 3.3.2. Failure Modes of Specimens in Group G1

Shear failure mode with one inclined cracking surface is observed under quasi-static compression. Only one pair of parallel flaws participate in the failure process, indicating that not all the defects in the specimen contribute to the failure under quasi-static loading.

Tensile failure mode under lower individual dynamic loading. The rock bridges in the middle of the specimen remain uncracked and retain their bearing capacity after dynamic loading.

Mixed tensile-shear failure under coupled static-dynamic loading. Diagonal shear cracks occur between the outer flaw tips, forming X-shaped conjugate shear bands; this result is similar to the those obtained by Feng et al. [25]. In addition, the dilatancy effect caused by the relative sliding of the shear bands results in secondary tensile cracks emerging from the outer flaw tips.

### 3.3.3. Failure Modes of Specimens in Group G2

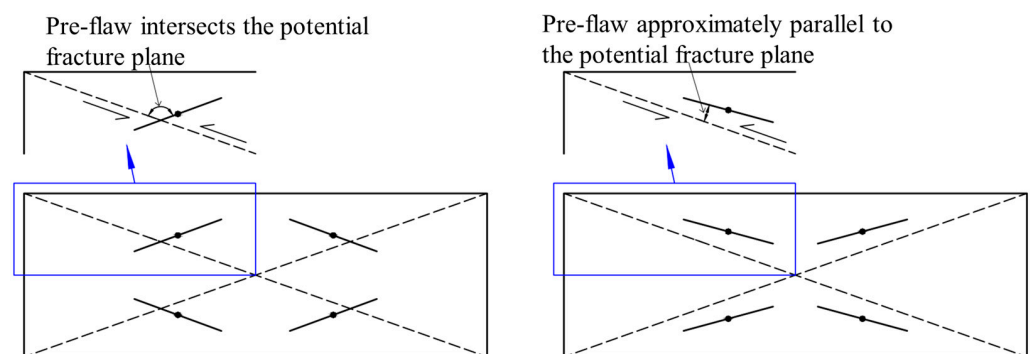
Mixed tensile-shear failure mode under quasi-static loading. After failure, the rock specimen generally breaks into three pieces: two triangle-shaped blocks and an hourglass-shaped block with local spalling in the middle.

Tensile failure mode dominated by wing cracks is observed in the low coupled static-dynamic loading, whose failure morphology is almost identical to that seen under quasi-static loading, but whose failure mechanism is different. The hourglass-shaped rock block in the middle remains uncracked, and retains its bearing capacity.

In the class of dynamic loading, as the pre-stress and dynamic stress increase, the failure mode transforms from tensile to shear failure. The dominant crack types alter from tensile wing cracks to coplanar shear cracks. The quasi-coplanar shear cracks initiated earlier than the tensile wing cracks under dynamic loading and coupled loading conditions, which is in accordance with the conclusions obtained by Feng and Zou [27,38].

In terms of specimen G2-50-0.6 subjected to higher pre-stress and dynamic stress, coplanar shear cracks coalesce between the horizontal inner flaw tips. Simultaneously, oblique shear cracks emerge at the same inner flaw tips and coalesce with each other between the vertical conjugate flaws. These two kinds of shear cracks jointly constitute a conjugate butterfly-shaped fracture zone. This pattern of failure is unique for the G2 specimens, and has not been observed in other loading conditions.

The inhibiting mechanism and enhancing mechanism of flaws on the X-shaped potential fracture planes under coupled loading may be determined from observations of the fracturing behaviors and failure modes of G0, G1, and G2, as indicated in Figure 10. It is found that the global fracture tendency of the rock sample is controlled by the loading conditions; when subjected to coupled loading, the potential shear fracture plane of the rock specimen is X-shaped, and the rock matrix on two sides of the shear plane has a tendency to slip.



**Figure 10.** Schematic diagram of the failure mechanism of G1 and G2 under coupled static-dynamic loading (The loading direction is horizontal).

The flaws that intersect the potential fracture plane (G1) will be compressed, inhibiting the shear slip of potential fracture planes and inducing the cracks to emerge at the stress concentration positions nearby (i.e., flaw tips). The new major fractures are the oblique shear cracks inclined with the flaws. For G2, the inclination angle of the flaw is approximately parallel to the X-shaped potential strain field. The set of flaw angles apparently enhances the potential shear slip. The shear slip between the rock matrix on the two sides of the flaw becomes the major fracture and induces quasi-coplanar shear to cracks appear at the flaw tips.

#### 3.4. Comparison of Failure Behaviors under Different Loading Conditions and Flaw Geometric Settings

Apparent differences in the distribution patterns of macro cracks between different test groups are observed. The fracturing behavior and failure modes are mainly affected simultaneously by the geometric setting of defects and the loading condition. A summary of the failure modes of intact and non-persistent conjugate-flawed white sandstone specimens under different loading conditions is illustrated in Table 4.

**Table 4.** Summary of failure modes of intact and non-persistent conjugate-flawed white sandstone specimens under different loading conditions.

Loading Condition	Specimen Group	G0	G1	G2	
		Pre-stress level	Loading rate/GPa·s <sup>-1</sup>	G0	G1
Quasi-static loading			T	S	T-S <sup>√1</sup>
Coupled static-dynamic loading	0%	1284–1483	-	T <sup>√</sup> -S	T <sup>√</sup> -S
	30%	1628–2081	<b>T</b>	T-S <sup>√</sup>	T-S <sup>√</sup>
		1275–1506	-	T-S <sup>√</sup>	T
	50%	1639–1893	<b>S</b>	T-S <sup>√</sup>	T-S <sup>√</sup>
		1257–1414	S	T-S <sup>√</sup>	T-S <sup>√</sup>
	1749–1982	S	T-S <sup>√</sup>	T-S <sup>√</sup>	

<sup>1</sup> The bold-faced letter with a superscript “√” indicates the dominant crack type in the mixed failure mode.

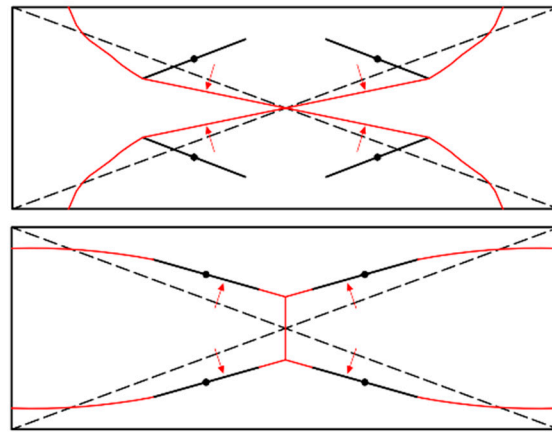
##### 3.4.1. The Influence of Loading Conditions

For non-persistent conjugate-flawed rock specimens in G1 and G2, the ultimate failure is generally dominated by the shear cracks under quasi-static loading and coupled loading. When subjected to quasi-static loading, the shear cracks tend to extend along the weak mechanical plane of the rock matrix, resulting in a curved propagation path, while under dynamic loading, the flaws could not propagate through the most vulnerable path in time. Numerous new cracks are simultaneously generated to externally dissipate the abundant energy input [4], leading to relatively flat shear planes. Therefore, when subjected to dynamic loading, it is observed in G1 that two conjugate and flat shear cracks appear simultaneously between the outer flaw tips, forming an X-shaped intersecting shear band. This also explains why spontaneous shear crack intersection is challenging to achieve under quasi-static loading but is commonly seen in dynamic tests [38,39]. On the other hand, as the pre-stress level increases, inclined shear cracks gradually dominate the failure behavior, indicating that the shear fracture gradually plays a vital role in rock failure because of the potential shear strain field induced by the high pre-stress.

##### 3.4.2. The Influence of Flaw Geometric Settings

Despite the opposite inclination angles of non-persistent conjugate flaws between G1 and G2, their failure modes are nearly the same. Except for tensile failure under lower dynamic loading, in most cases, the rock specimens exhibit mixed tensile-shear failure dominated by shear fracture. When subjected to coupled static-dynamic loading, the shear failure mode with X-shaped shear belts occurs in both G1 and G2, which is similar to

the failure modes of the conjugate-flawed rock specimens identified by [4]. Figure 11 displays the schematic diagram of the representative distribution morphology of the major fracturing planes of G1 and G2 under coupled static-dynamic loading. The black dotted line is the main shear crack of the intact specimen without flaws, and the red line is the main shear crack of the non-persistent conjugate-flawed specimens. In group G1, the shear cracks emerge at the outer flaw tips and propagate through the rock bridge in the center, forming X-shaped shear bands with more gentle inclined angles. In G2, the flaws are almost parallel with the black dotted potential shear planes. The actual shear cracks extend along the paths coplanar or quasi-coplanar to the flaws and eventually develop into X-shaped conjugate shear cracks.



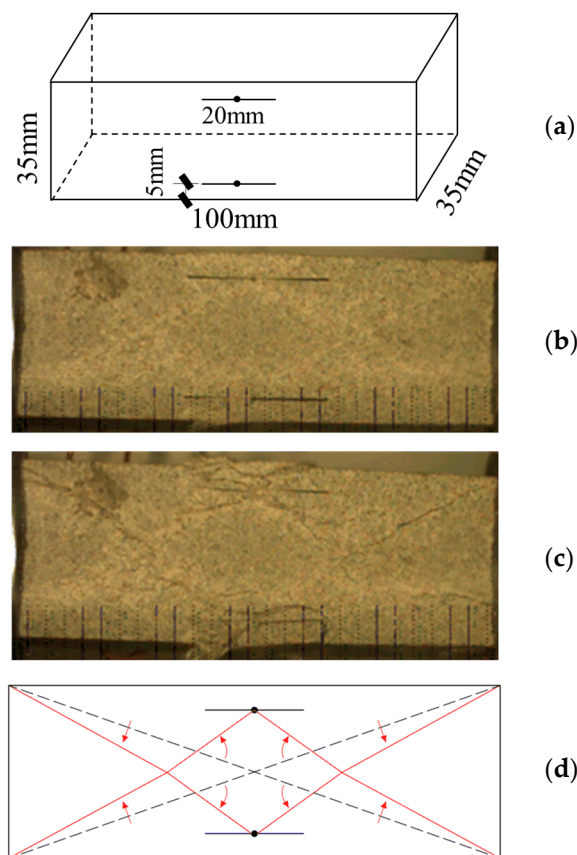
**Figure 11.** Schematic diagram of the representative distribution morphology of the major fracturing plane of G1 and G2 under coupled static-dynamic loading (the loading direction is horizontal).

### 3.5. Guiding Effect of Pre-Flaws

The existence of natural defects and flaws, with several scales and geometries, is one of the critical factors that control the fracturing behavior and the local failure mechanism of the rock mass. New cracks generally initiate at the tips of natural defects, then propagate through rock bridge regions, resulting in the ultimate failure of rock. The effects of non-persistent conjugate flaws on the fracturing behavior and the failure mechanism of rock are experimentally investigated.

In Figure 11, it can be observed that the shear cracks' morphology is essentially based on the X-shaped black lines. The existence of flaws results only in the deviation and deformation of the shear cracks, to some extent. From the perspective of localized analysis, the flaws affect the X-shaped potential fracture planes by the inhibiting mechanism and enhancing mechanism in G1 and G2, respectively, which induce different types of cracks. Both mechanisms can be determined as the "guiding effects" of flaws on fracture planes. However, from an overall point of view, X-shaped shear cracks always dominate the failure, regardless of the opposite inclination angles of the flaws or the crack types.

To verify the conclusion above that the shear cracks' morphology is essentially based on the X-shaped shear bands, the existence of flaws only results in deviation and deformation of the shear cracks, to some extent (i.e., guiding effect), we conducted supplementary experiments on a white sandstone specimen with two parallel flaws; the experimental results are shown in Figure 12. Two parallel flaws, 20 mm in length, are prefabricated at the position 5 mm from the top and bottom boundary of the rock specimen. The pre-stress level and dynamic loading rate are 50% (46.70 MPa) and 1819 GPa·s<sup>-1</sup>, respectively. The Supplementary Material contains two tables which demonstrate the geometrical dimensions, loading conditions, and failure modes of each white sandstone specimen.



**Figure 12.** Supplementary experiment: (a) illustration of the geometry of the parallel-flawed rock specimen; (b) distribution of white patches; (c) failure image; (d) schematic diagram of the major fracture plane. (The loading direction is horizontal).

Figure 12b,c depicts the white patch distribution and the fracturing behavior of the parallel-flawed rock specimen under static-dynamic loading. It can be observed that the failure mode is dominated by shear cracking, and the fracture morphology is unique, with double X-shaped shear belts formed by the influence of the two parallel flaws, resulting in a diamond-shaped rock block remaining in the center. The schematic diagram of the major fracture plane is shown in Figure 12d, and it reveals that the shear cracks intending to coalesce in the middle of the specimen are guided by the flaws and deflect towards them. The large angular deflection of the shear cracks in this test verifies the validity of the “guiding effect” of preexisting defects on shear cracking. This is probably because the cracking behavior is strongly correlated with stress concentration area, where the rock matrix is more likely to overcome the surface free energy.

Generally speaking, the loading condition dominates the fracture tendency of rock macroscopically, while the geometric setting of defects significantly affects the regional fracturing behavior and the failure mode locally. In particular, under the shear failure mode, the distribution morphology of the major shear crack is mainly controlled by the loading condition, and the existence of the preexisting defects or flaws only shift its morphology, to a certain extent; that is, the defects exert a specific “guiding effect” on the growth of the main crack, but cannot change its macroscopic direction. More detailed studies are needed in the future to further comprehensively investigate the mechanism of this “guiding effect” of flaws.



#### 4. Conclusions

This study investigated the dynamic fracturing behavior and the failure mechanism of non-persistent conjugate-flawed rock specimens. The main conclusions can be drawn as follows:

1. There are significant differences in the coalescence patterns between the conjugate flaws in rock under quasi-static and dynamic loading. Regardless of the configuration of the conjugate flaws, tensile cracks and shear cracks dominate the failure behavior under quasi-static and dynamic loading, respectively.
2. The non-persistent conjugate-flawed rock failed in the tensile-shear mixed failure mode in our dynamic tests. The macro failure behaviors usually consist of two or more crack coalescence patterns. With increasing pre-stress ratio, the dominating cracks transfer from tensile cracks to shear cracks.
3. Two kinds of pre-flaw influencing mechanisms on the rock failure mechanism are observed. The flaw intersecting with the potential shear fracture plane is subjected to compression and exhibits an inhibiting mechanism against the global fracture behavior. The flaw approximately parallel to the potential shear strain field intensifies the shear fracture, representing the enhancing mechanism.
4. Generally, the loading condition dominates the fracture tendency of rock macroscopically, while the geometric setting of defects significantly affects the regional fracturing behavior and failure mode locally. Specifically, the pre-flaw has a guiding effect on the development of fracture, which results in the deviation and deformation of shear cracks.

**Supplementary Materials:** The following supporting information can be downloaded at: <https://www.mdpi.com/article/10.3390/su15043637/s1>, Table S1: Geometrical dimensions and loading conditions of white sandstone specimens; Table S2: The failure modes of intact and intermittent conjugate-flawed white sandstone specimens under different loading conditions (The loading direction is horizontal).

**Author Contributions:** Conceptualization, Z.L.; methodology, S.X.; data curation, S.X.; formal analysis, Q.S., P.W. and D.L.; investigation, Q.S., P.W. and K.X.; writing—original draft, Z.L., S.X. and D.L. All authors have read and agreed to the published version of the manuscript.

**Funding:** This research was funded by the Natural Science Foundation of Chongqing, (cstc2020jcyjmsxmX0558 and cstc2020jcyjmsxmX0567), the Open Fund of Chongqing Key Laboratory of Energy Engineering Mechanics, and Disaster Prevention and Reduction (Grant No. EEMDPM2021206), the Postgraduate Innovation Program of Chongqing University of Science and Technology (YKJCX2120660 and YKJCX2120661), and the Science and Technology Research Program of Chongqing Municipal Education Commission (No. KJZD-K202101505).

**Institutional Review Board Statement:** Not applicable.

**Informed Consent Statement:** Not applicable.

**Data Availability Statement:** The data used to support the findings of this study are available from the corresponding author upon request.

**Acknowledgments:** The authors would like to thank the laboratory and the university for their support.

**Conflicts of Interest:** The authors declare no conflict of interest.

#### References

1. Feng, P.; Dai, F.; Liu, Y.; Xu, N.; Fan, P. Effects of Coupled Static and Dynamic Strain Rates on the Mechanical Behaviors of Rock-Like Specimens Containing Preexisting Fissures under Uniaxial Compression. *Can. Geotech. J.* **2018**, *55*, 640–652. [CrossRef]
2. Najm, S.J.; Daraei, A. Forecasting and controlling two main failure mechanisms in the Middle East's longest highway tunnel. *Eng. Fail. Anal.* **2023**, *146*, 107091. [CrossRef]
3. Pollard, D.D.; Aydin, A. Progress in understanding jointing over the past century. *Gsa Bull.* **1988**, *100*, 1181–1204. [CrossRef]
4. Feng, P.; Zhao, J.; Dai, F.; Wei, M.; Liu, B. Mechanical behaviors of conjugate-flawed rocks subjected to coupled static–dynamic compression. *Acta Geotech.* **2021**, *17*, 1765–1784. [CrossRef]

5. Tang, C.A.; Lin, P.; Wong, R.H.C.; Chau, K.T. Analysis of crack coalescence in rock-like materials containing three flaws-Part I experimental approach. *Int. J. Rock Mech. Min. Sci.* **2001**, *38*, 925–939. [[CrossRef](#)]
6. Reyes, O.; Einstein, H.H. Failure mechanisms of fractured rock—A fracture coalescence model. In Proceedings of the 7th ISRM International Congress on Rock Mechanics, Aachen, Germany, 16 September 1991.
7. Wong, R.; Chau, K.T. Crack coalescence in a rock-like material containing two cracks. *Int. J. Rock Mech. Min. Sci.* **1998**, *35*, 147–164. [[CrossRef](#)]
8. Zhao, C.; Zhou, Y.; Zhao, C.; Bao, C. Cracking Processes and Coalescence Modes in Rock-Like Specimens with Two Parallel Pre-existing Cracks. *Rock Mech. Rock Eng.* **2018**, *51*, 3377–3393. [[CrossRef](#)]
9. Lin, Q.; Cao, P.; Wen, G.; Meng, J.; Cao, R.; Zhao, Z. Crack coalescence in rock-like specimens with two dissimilar layers and pre-existing double parallel joints under uniaxial compression. *Int. J. Rock Mech. Min. Sci.* **2021**, *139*, 104621. [[CrossRef](#)]
10. Zhang, X.-P.; Liu, Q.; Wu, S.; Tang, X. Crack coalescence between two non-parallel flaws in rock-like material under uniaxial compression. *Eng. Geol.* **2015**, *199*, 74–90. [[CrossRef](#)]
11. Li, C.; Prikryl, R.; Nordlund, E. The stress-strain behaviour of rock material related to fracture under compression. *Eng. Geol.* **1998**, *49*, 293–302. [[CrossRef](#)]
12. Cao, R.-H.; Cao, P.; Fan, X.; Xiong, X.; Lin, H. An Experimental and Numerical Study on Mechanical Behavior of Ubiquitous-Joint Brittle Rock-Like Specimens Under Uniaxial Compression. *Rock Mech. Rock Eng.* **2016**, *49*, 4319–4338. [[CrossRef](#)]
13. Yin, P.; Wong, R.H.C.; Chau, K.T. Coalescence of two parallel pre-existing surface cracks in granite. *Int. J. Rock Mech. Min. Sci.* **2014**, *68*, 66–84. [[CrossRef](#)]
14. Zhang, B.; Li, Y.; Yang, X.Y. Influence of Two Cross-Flaws Geometry on the Strength and Crack Coalescence of Rock-Like Material Specimens under Uniaxial Compression. *Int. J. Geomech.* **2020**, *20*, 04020134. [[CrossRef](#)]
15. Sharafisafa, M.; Aliabadian, Z.; Tahmasebinia, F.; Shen, L. A comparative study on the crack development in rock-like specimens containing unfilled and filled flaws. *Eng. Fract. Mech.* **2021**, *241*, 107405. [[CrossRef](#)]
16. Zhou, X.; Lian, Y.; Wong, L.; Berto, F. Understanding the fracture behavior of brittle and ductile multi-flawed rocks by uniaxial loading by digital image correlation. *Eng. Fract. Mech.* **2018**, *199*, 438–460. [[CrossRef](#)]
17. Cao, P.; Liu, T.; Pu, C.; Lin, H. Crack propagation and coalescence of brittle rock-like specimens with pre-existing cracks in compression. *Eng. Geol.* **2015**, *187*, 113–121. [[CrossRef](#)]
18. Wong, R.; Chau, K.T. The coalescence of frictional cracks and the shear zone formation in brittle solids under compressive stresses. *Int. J. Rock Mech. Min. Sci.* **1997**, *34*, 335. [[CrossRef](#)]
19. Wong, L.N.Y.; Einstein, H.H. Crack Coalescence in Molded Gypsum and Carrara Marble: Part 2—Microscopic Observations and Interpretation. *Rock Mech. Rock Eng.* **2008**, *42*, 513–545. [[CrossRef](#)]
20. Feng, P.; Dai, F.; Shuai, K.; Wei, M. Dynamic mechanical behaviors of pre-fractured sandstone with noncoplanar and unparallel flaws. *Mech. Mater.* **2022**, *166*, 104219. [[CrossRef](#)]
21. Li, D.; Han, Z.; Sun, X.; Zhou, T.; Li, X. Dynamic Mechanical Properties and Fracturing Behavior of Marble Specimens Containing Single and Double Flaws in SHPB Tests. *Rock Mech. Rock Eng.* **2018**, *52*, 1623–1643. [[CrossRef](#)]
22. Yan, Z.; Dai, F.; Liu, Y.; Du, H.; Luo, J. Dynamic Strength and Cracking Behaviors of Single-Flawed Rock Subjected to Coupled Static–Dynamic Compression. *Rock Mech. Rock Eng.* **2020**, *53*, 4289–4298. [[CrossRef](#)]
23. Yue, Z.; Peng, L.; Yue, X.; Wang, J.; Lu, C. Experimental study on the dynamic coalescence of two-crack granite specimens under high loading rate. *Eng. Fract. Mech.* **2020**, *237*, 107254. [[CrossRef](#)]
24. Zhou, X.; Gu, S. Dynamic mechanical properties and cracking behaviours of persistent fractured granite under impact loading with various loading rates. *Theor. Appl. Fract. Mech.* **2022**, *118*, 103281. [[CrossRef](#)]
25. Feng, P.; Liu, B.; Tang, R.; Wei, M.; Zhang, Y.; Li, H. Dynamic fracture behaviors and fragment characteristics of pre-compressed flawed sandstones. *Int. J. Mech. Sci.* **2022**, *220*, 107162. [[CrossRef](#)]
26. Li, D.; Gao, F.; Han, Z.; Zhu, Q. Experimental evaluation on rock failure mechanism with combined flaws in a connected geometry under coupled static-dynamic loads. *Soil Dyn. Earthq. Eng.* **2020**, *132*, 106088. [[CrossRef](#)]
27. Feng, P.; Xu, Y.; Dai, F. Effects of dynamic strain rate on the energy dissipation and fragment characteristics of cross-fissured rocks. *Int. J. Rock Mech. Min. Sci.* **2021**, *138*, 104600. [[CrossRef](#)]
28. Yan, Z.; Dai, F.; Zhu, J.; Xu, Y. Dynamic Cracking Behaviors and Energy Evolution of Multi-flawed Rocks under Static Pre-compression. *Rock Mech. Rock Eng.* **2021**, *54*, 5117–5139. [[CrossRef](#)]
29. Zhu, Q.; Li, D.; Han, Z.; Xiao, P.; Li, B. Failure characteristics of brittle rock containing two rectangular holes under uniaxial compression and coupled static-dynamic loads. *Acta Geotech.* **2021**, *17*, 131–152. [[CrossRef](#)]
30. Yan, Z.; Dai, F.; Liu, Y.; Li, Y.; You, W. Experimental investigation of flawed rocks under combined static-dynamic loading: Mechanical responses and fracturing characteristics. *Int. J. Mech. Sci.* **2021**, *211*, 106755. [[CrossRef](#)]
31. Shu, P.; Li, H.; Wang, T.; Ueng, T. Dynamic strength of rock with single planar joint under various loading rates at various angles of loads applied. *J. Rock Mech. Geotech. Eng.* **2018**, *10*, 545–554. [[CrossRef](#)]
32. Feng, P.; Wei, M.; Dai, F.; Tang, R.; Qiu, H.; Gong, J. DEM investigation on the mechanical behaviors of flawed specimens subjected to coupled static-dynamic loads. *Soil Dyn. Earthq. Eng.* **2020**, *135*, 106220. [[CrossRef](#)]
33. Yan, Z.; Dai, F.; Liu, Y.; Du, H. Experimental investigations of the dynamic mechanical properties and fracturing behavior of cracked rocks under dynamic loading. *Bull. Eng. Geol. Environ.* **2020**, *79*, 5535–5552. [[CrossRef](#)]

34. Zhou, Z.; Cai, X.; Li, X.; Cao, W.; Du, X. Dynamic Response and Energy Evolution of Sandstone Under Coupled Static–Dynamic Compression: Insights from Experimental Study into Deep Rock Engineering Applications. *Rock Mech. Rock Eng.* **2019**, *53*, 1305–1331. [[CrossRef](#)]
35. Li, X.; Zhou, Z.; Lok, T.-S.; Hong, L.; Yin, T. Innovative testing technique of rock subjected to coupled static and dynamic loads. *Int. J. Rock Mech. Min. Sci.* **2008**, *45*, 739–748. [[CrossRef](#)]
36. Han, Z.; Li, D.; Li, X. Experimental study on the dynamic behavior of sandstone with coplanar elliptical flaws from macro, meso, and micro viewpoints. *Theor. Appl. Fract. Mech.* **2022**, *120*, 104326. [[CrossRef](#)]
37. Zhou, Y.; Xia, K.; Li, X. Suggested methods for determining the dynamic strength parameters and mode-I fracture toughness of rock materials. *Int. J. Rock Mech. Min. Sci.* **2012**, *49*, 105–112. [[CrossRef](#)]
38. Zou, C.; Li, J.; Zhao, X.; Zhao, J. Why are tensile cracks suppressed under dynamic loading?—Transition strain rate for failure mode. *Extrem. Mech. Lett.* **2021**, *49*, 101506. [[CrossRef](#)]
39. Zou, C.; Li, H. Combined numerical and experimental studies on the dynamic and quasi-static failure modes of brittle rock. *Int. J. Rock Mech. Min. Sci.* **2021**, *148*, 104957. [[CrossRef](#)]

**Disclaimer/Publisher’s Note:** The statements, opinions and data contained in all publications are solely those of the individual author(s) and contributor(s) and not of MDPI and/or the editor(s). MDPI and/or the editor(s) disclaim responsibility for any injury to people or property resulting from any ideas, methods, instructions or products referred to in the content.